Grid-forming Control Based on Adaptive Reactive Power Allocation for Offshore Wind Farms Connected to Diode-rectifier-based HVDC System

Ganghua Zhang, Wang Xiang, Xia Chen, Rui Tu, Xuebo Qiao, and Jinyu Wen

***Abstract*—Diode-rectifier-based high-voltage direct current (DR-HVDC) systems are considered an attractive solution for integrating offshore wind farms (OWFs). Grid-forming (GFM) control with a rational reactive power allocation capability is crucial for the safe operation of numerous wind turbines (WTs). Most typical GFM controls aim to share surplus reactive power of the system equally among WTs, easily rendering capacity overloads for WTs that are outputting high levels of active power. In this paper, a novel GFM control for OWFs is proposed, allowing for adaptively allocating the reactive power according to the actual active power output of WTs. Firstly, the reactive power characteristics of the AC collection networks and WTs are analyzed across a wide wind power range. Then, combining the positive correlation of WT active power with the output AC voltage, a *Q*-θ type GFM control for WTs is presented. The adaptive reactive power allocation mechanism and the parameter design of the *Q*- θ based reactive power controller are elucidated, ensuring that WTs with lower active power output contribute more reactive power to the system than WTs with higher active power output. The AC impedance models of WTs under various GFM controls are established to evaluate the impact of different reactive power controllers. Finally, the feasibility of the proposed control is validated in PSCAD/EMTDC, accompanied by stability analysis.**

***Index Terms*—Offshore wind farm, diode-rectifier, high-voltage direct current (HVDC), grid-forming control, reactive power allocation, stability analysis.**

I. Introduction

OFFSHORE wind power has been widely recognized for its abundant resource potential [1]. As the grid-connected scale expands, there is a notable shift towards far-sea locations. The capacitive effects of transmitting wind power over extended distances diminish the advantages of high-voltage alternating current technology [2]. In this regard, high-voltage direct current (HVDC) transmission systems are increasingly favored for integrating offshore wind farms (OWFs) over medium- and long-distances [3]. The modular multilevel converter (MMC) based HVDC systems exhibit high control flexibility and are prevalently adopted in existing OWF projects. Nonetheless, their deployment necessitates expensive and heavy offshore platforms with notable operational losses, posing substantial barriers to widespread adoption [4].

Recently, diode-rectifier-based HVDC (DR-HVDC) systems have garnered considerable attention with the superiority of light-duty and cost-effective converters [5], [6]. And these systems hold promising prospects for OWF integration. However, their uncontrolled diode characteristics limit their grid-forming (GFM) capability in the AC collection networks [7]. To address this limitation, additional active equipment such as auxiliary MMC can be employed [8], albeit at the expense of diminishing the economic benefits of diode rectifiers (DRs). Notably, the grid-side converters (GSCs) of wind turbines (WTs) inherently possess excellent control capabilities. As an alternative to the conventional grid-following (GFL) control scheme, WTs can play a pivotal role in forming the AC voltage of the AC collection networks. Thus, it can compensate for the lack of voltage support and reactive power balance in GFL type WTs, contributing to improved system stability [9]. For DR-HVDC systems, GFM controls for WTs typically involve centralized GFM control [10] - [12], distributed phase-locked loop (PLL) type GFM control [13], [14], self-synchronizing type GFM control [15], [16] and similar variants.

In [10], a centralized GFM control for WTs is proposed, achieving voltage and frequency regulation through active and reactive power control loops. But this approach relies on rapid communication among WTs for grid connection and AC voltage control at the point of common coupling (PCC). In [11], a *Q*-θ and *P*-*V* based GFM control structure employing proportional-integral (PI) controllers is developed with fixed reference frequencies of each WT. Hence, synchroniza-

Manuscript received: July 14, 2024; revised: November 2, 2024; accepted: December 5, 2024. Date of CrossCheck: December 5, 2024. Date of online publication: January 30, 2025.

This work was supported by the National Key Research and Development Program of China (No. 2022YFB2405400) and in part by the National Natural Science Foundation of China (No. 52237004).

G. Zhang, W. Xiang (corresponding author), X. Chen, R. Tu, X. Qiao, and J. Wen are with the School of Electrical and Electronic Engineering, Huazhong University of Science and Technology, Wuhan 430074, China (e-mail: hustzghua@foxmail.com; xiangwang1003@hust.edu.cn; cxhust@foxmail.com; turui_hust@foxmail.com; qiaoxb@csg.cn; jinyu.wen@ hust.edu.cn).

DOI: 10.35833/MPCE.2024.00743

tion during startup of WTs can be facilitated by an internal global positioning system, yet it remains reliant on communication to allocate reactive power [12]. To minimize the reliance on communication links, distributed PLL type GFM controls are introduced in [13] and [14], enabling smooth startup of WTs. The reactive power in the AC collection networks is evenly allocated through *Q-f* droop control.

Given the potential destabilizing effects of additional PLLs on OWFs, a *Q-f* based self-synchronizing type GFM control (i.e., *Q-f* type GFM control) is explored in [15]. The operational mechanism of GFM-controlled WTs is elaborated in [16] through the sensitivity analysis. The reactive power allocation result is identical to that under the PLL type GFM control. However, since some WTs frequently reach full power [17], while their reactive power output remains the same as that of the WTs with lower active power output, there is a risk of capacity overload for WTs with higher active power output and underutilization for WTs with lower active power output [18]. Moreover, since DRs and their AC transformers need to absorb a substantial amount of reactive power (up to 0.4 p.u.), it is necessary to configure and switch AC filter banks (AFBs) in groups to meet the reactive power demand at the varying wind power levels [19]. Therefore, with the switching or even maloperation of AFBs, the above-mentioned overload issues of WTs will be potentially exacerbated by the large fluctuations in the reactive power of the system [20]. As a result, the rated capacity of WT GSCs must be increased under the above GFM controls, raising the equipment cost. In addition, the stability of DR-HVDC systems under various GFM controls with different reactive power controllers remains inadequately studied, particularly the instability mechanism of distributed PLL type GFM control. To tackle these challenges, this paper presents a novel GFM control for OWFs connected to the DR-HVDC system, which improves the reactive power allocation. The major contributions are as follows.

1) A *Q-θ* type GFM control of WTs is proposed to optimally and adaptively allocate reactive power according to their actual active power, effectively precluding the overload of the WT GSC without increasing the rated capacity under varying conditions.

2) The impact of different reactive power controllers under different GFM controls on the stability of DR-HVDC systems is revealed, which recommends the conservative reactive power control parameter settings to mitigate negative damping.

3) The potential risk of high-frequency oscillations in the distributed PLL type GFM control, which results from the additional control delay introduced by a PLL-based AC voltage controller, is highlighted.

The remainder of the paper is outlined as follows. Section II illustrates the system configuration and operating characteristics of the DR-HVDC based OWF integration system. In Section III, a *Q-θ* type GFM control of WTs based on adaptive reactive power allocation is presented, and the mechanism of reactive power allocation among WTs is analyzed. Moreover, Section IV presents the sequence impedance modeling of wind farms under different GFM controls. The feasibility of the proposed control and system stability are validated by simulations in Section V. Finally, Section VI provides the conclusion.

II. System Configuration and Operating Characteristics of DR-HVDC Based OWF Integration System

A. Topology Structure

Figure 1 illustrates the topology of the DR-HVDC based OWF integration system, consisting of OWFs, an offshore platform, and an onshore station. The OWFs are composed of ten WT strings connected in parallel to PCC via AC collection cables. Each string comprises ten WTs with a rated capacity of 10 MW. The permanent magnet synchronous generator based WT is adapted to operate in GFM mode to provide voltage and frequency for AC collection networks. Two diode-based 12-pulse DRs rectify the wind power output and transmit it to onshore MMC through DC cables. The DC voltage of the DR-HVDC link is regulated by the onshore MMC using a fixed DC voltage control.

In light of the fact that the reactive power compensation of DRs is implemented by WTs, the rated capacity of WT GSCs and AC transformers must be increased by approximately 6.5% [19], which increases the equipment cost. Consequently, bank-controlled AC filters are configured at the PCC to meet the full compensation and filtering requirements of reactive power of DRs. This is also advantageous for providing a portion of wind power under AC collection network faults on the WT side. Hence, WTs in this paper do not require additional capacity.

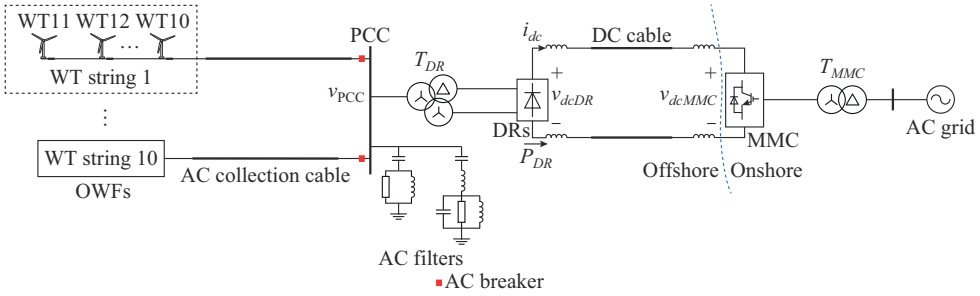

Fig. 1. Topology of DR-HVDC based OWF integration system.

Considering the impact of the leakage inductance of the AC transformer T_{DR} on the DR commutation process, the voltage relationship between the AC and DC sides of DRs is expressed in (1) with reference to [15].

$$v_{dcDR}=\frac{6\sqrt{6}\,k_{DR}V_{PCC}}{\pi}-\frac{6k_{DR}^2\omega_1 L_{TDR}i_{dc}}{\pi} \tag{1}$$

where v_{dcDR} and i_{dc} are the DC voltage and DC current of DRs, respectively; V_{PCC} is the root mean square (RMS) value of PCC phase voltage v_{PCC}; ω_1 is the rated angular frequency; k_{DR} is the AC transformer ratio of T_{DR}; and L_{TDR} is the leakage inductance of T_{DR}.

Based on (1), the transmitted active power P_{DR} of DRs can be written in (2), ignoring the loss of the rectifier and the HVDC link [15]. It is evident that there is a tight positive correlation between V_{PCC} and P_{DR} when v_{dcMMC} is fixed.

$$P_{DR}=v_{dcDR}i_{dc}=\frac{\sqrt{6}\,v_{dcMMC}}{k_{DR}\omega_1 L_{TDR}}V_{PCC}-\frac{\pi v_{dcMMC}^2}{6k_{DR}^2\omega_1 L_{TDR}} \tag{2}$$

where v_{dcMMC} is the DC voltage of onshore MMC.

According to the characteristics of DRs in [21], the reactive power Q_{DR} absorbed by T_{DR} and commutation is obtained as:

$$Q_{DR}=P_{DR}\tan\varphi \tag{3}$$

$$\cos\varphi=0.5(1+\cos\mu)=1-k_{DR}\omega_1 L_{TDR}i_{dc}/(\sqrt{6}\,V_{PCC}) \tag{4}$$

where μ and φ are the DR commutation angle and power factor angle, respectively.

B. Reactive Power Characteristics of AC Collection Networks

Figure 2 depicts the diagram of the reactive power distribution within the AC collection networks. The AC collection cables are modeled as equivalent π circuits [22].

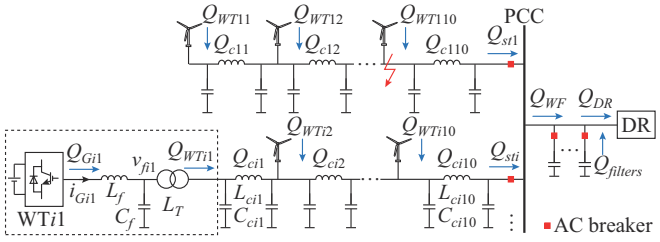

Fig. 2. Diagram of reactive power distribution within AC collection networks.

In Fig. 2, it is assumed that the AC collection cables from WTi1 ($i=1,2,\ldots,10$) to WTi9 at WT string i have the same length of x. Considering the demands of the DR platform and OWF spacing, the length of AC collection cables between WTi10 and PCC bus is y_i. The equivalent inductance and capacitance of AC collection cable j ($j=1,2,\ldots,10$) at WT string i are L_{cij} and C_{cij}, respectively, while the equivalent resistance R_{cij} is not drawn in Fig. 2.

Denote the reactive power generated by OWFs and AC filters as Q_{WF} and $Q_{filters}$, respectively. The balance of reactive power on the PCC side is satisfied in (5)-(7). As derived in (6), the reactive power components Q_{sti} in OWFs originate in each series of WT string i.

$$Q_{WF}+Q_{filters}=Q_{DR} \tag{5}$$

$$Q_{WF}=\sum_{i=1}^{10}Q_{sti}=\sum_{i=1}^{10}\sum_{j=1}^{10}(Q_{WTij}+Q_{cij}) \tag{6}$$

$$Q_{filters}=nQ_{bank} \tag{7}$$

where Q_{WTij} is the reactive power generated by WT j at WT string i; Q_{cij} is the reactive power generated by AC collection cable j at WT string i; n is the number of AFBs in operation; and Q_{bank} is the reactive power capacity per bank.

Take WTij at WT string i as an example. Regardless of the effect of capacitor reactive current on the voltage drop of a series branch, Q_{WTij} and Q_{cij} in (6) can be further expressed as:

$$Q_{WTij}=Q_{Gij}+3\omega_1 C_f V_{fij}^2-3\omega_1(L_f+L_T)I_{Gij}^2 \tag{8}$$

$$Q_{cij}=6\omega_1 C_{cij}V_{fij}^2-3\omega_1 L_{cij}\left(\sum_j I_{Gij}\right)^2 \tag{9}$$

where Q_{Gij} is the reactive power generated in the GSC of WT j at WT string i; V_{fij} and I_{Gij} are the RMS values of phase voltage v_{fij} and current i_{Gij} in the GSC of WT j at WT string i, respectively; L_f and C_f are the inductance and capacitance of LC filters in WTs, respectively; and L_T is the leakage inductance of AC step-up transformer.

As analyzed in (8) and (9), the reactive power generated in the AC collection networks Q_{AC} can be defined as:

$$Q_{AC}=\sum_{i=1}^{10}\sum_{j=1}^{10}[3\omega_1 C_f V_{fij}^2-3\omega_1(L_f+L_T)I_{Gij}^2+Q_{cij}] \tag{10}$$

Based on (3) and (10), Fig. 3 displays the reactive power characteristics of DRs and the AC collection networks in various wind power scenarios. The parameters of the DR-HVDC based OWF integration system are listed in Table I, where R_{hp}, L_{hp}, and C_{hp} are the resistance, inductance, and capacitance of the high-pass filter in an AFB, respectively; L_1 and C_1 are the inductance and capacitance of the double-tuned filter connected in series in an AFB, respectively; and R_2, L_2, and C_2 are the resistance, inductance, and capacitance of the double-tuned filter connected in parallel in an AFB, respectively.

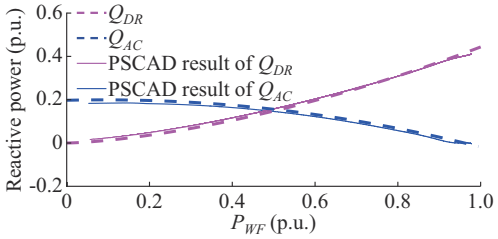

Fig. 3. Reactive power characteristics of DRs and AC collection networks in various wind power scenarios.

It is shown that the reactive power Q_{DR} and Q_{AC} calculated in (3) and (10) are basically consistent with the simulation results in PSCAD. The AC collection networks exhibit a capacitive characteristic that is enhanced as the wind power P_{WF} decreases [22]. Under rated power operating conditions, the demand for reactive power of DRs reaches a maximum value of approximately 0.4 p. u.. Q_{DR} decreases rapidly as P_{WF} decreases. Even if P_{WF} drops to 0.48 p. u., the system

will generate excess reactive power without accounting for the reactive power compensation effect of AFBs.

TABLE I
PARAMETERS OF DR-HVDC BASED OWF INTEGRATION SYSTEM

Quantity	Value	Quantity	Value
Rated wind power	1000 MW	L_f	0.15 p.u.
Rated frequency f_1	50 Hz	C_f	0.08 p.u.
Rated PCC voltage	66 kV	$L_{ci1\text{-}9}$, L_{ci10}	0.001 H, 0.01 H
k_{DR}	3.92	$C_{ci1\text{-}9}$, C_{ci10}	0.33 μF, 3.3 μF
L_{TDR}	0.18 p.u.	$R_{c1\text{-}9}$, R_{c10}	0.038 Ω, 0.38 Ω
L_T	0.07 p.u.	x, y_i	2 km, 20 km
R_{hp}, L_{hp}, C_{hp}	5.1 Ω, 0.96 mH, 36.5 μF	L_1, C_1, R_2, L_2, C_2	2 mH, 36.5 μF, 200 Ω, 0.05 mH, 1405 μF

C. Issues with Q-f Type GFM Control

According to (5) - (10), denote Q_{Gtot} as the sum of Q_{Gij}, which can be written in (11). It can be observed that the variation of Q_{Gtot} contains the variation of Q_{DR}, Q_{AC}, and $Q_{filters}$, which is predominantly attributable to wind power fluctuations and AFB switching.

$$Q_{Gtot}=\sum_{i=1}^{10}\sum_{j=1}^{10}Q_{Gij}=Q_{DR}-Q_{AC}-Q_{filters} \tag{11}$$

Under the *Q-f* type GFM control and distributed PLL type GFM control, the total reactive power demand is balanced equally by each WT based on its rated capacity. Since the frequency f_G of v_{PCC} is a common feature for all WTs, the equal reactive power allocation of WTs can be achieved by a *Q-f* droop controller with the same reactive power reference and droop coefficient, shown as:

$$(Q_{Gij}-Q_{Gref})k_Q=2\pi(f_G-f_1) \tag{12}$$

where Q_{Gref} is the reference of Q_{Gij}; and k_Q is the proportional gain.

Figure 4 illustrates the reactive power characteristics of *Q-f* droop based GFM-type WTs considering abnormal conditions of AFBs. Given that the ratio of AFBs in filter is greater than 20% [18], the maximum number of AFBs is designed to be 4 to avoid the frequent switching of AFBs. The switching thresholds of 3 AFBs are set to be 0.86 p.u., 0.73 p.u., 0.58 p.u., while the switching logic of the remaining one is not set, which is always in operation to ensure PCC voltage quality.

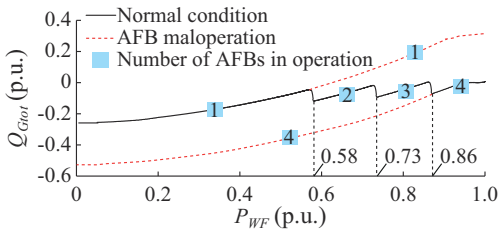

Fig. 4. Reactive power characteristics of *Q-f* droop based GFM-type WTs considering abnormal conditions of AFBs.

It can be observed that WT GSCs are required to absorb the surplus reactive power under normal operation. When the aggregated wind power output of OWFs is less than 0.4 p.u., Q_{Gtot} equally balanced by each WT falls below –0.15 p.u.. When a conventional *Q-f* droop controller is used, even WTs operating at the rated wind power are forced to share the reactive power equally. It poses a risk of overloading the WT. In particular, as shown by red dotted lines in Fig. 4, the erroneous switching of 3 AFBs either on or off aggravates the issue, necessitating WTs to absorb or generate more reactive power.

III. *Q-θ* Type GFM Control of WTs Based on Adaptive Reactive Power Allocation and Mechanism of Reactive Power Allocation Among WTs

A. Q-θ Type GFM Control of WTs Based on Adaptive Reactive Power Allocation

In general, WTs need to achieve the maximum power point tracking (MPPT) of wind power generation and control the DC voltage inside.

Due to the uncontrollable nature of DRs, WTs also need to generate AC voltage and frequency and regulate the balance of reactive power in the AC collection network. Given that the DC voltage of WT is maintained by its machine-side converter (MSC), the voltage of WT DC link can be decoupled from the grid side, minimizing the interaction effects [23]. The DC voltage control of WT MSC adopted in this paper refers to [12]. Consequently, it is crucial for WT GSC to control the active power and reactive power in the GFM mode.

As evaluated in Fig. 4, WTs with higher active power output are susceptible to capacity overloads, which are more severe under AFB maloperation conditions. Hence, an approach is proposed in this paper that adaptively allocates reactive power based on the actual active power output of WTs. Concretely, WTs with lower active power output contribute more reactive power, while WTs with higher active wind power output contribute less reactive power.

Figure 5 depicts the diagram of a novel *Q-θ* type GFM control based on adaptive reactive power allocation for WT GSCs. It consists of a dual-loop PI controller, a *P-V* PI controller, a *Q-θ* based reactive power controller, and an enabling controller for capacity limitation. The dual-loop PI controller is responsible for voltage formation in the AC collection network and overcurrent protection during system faults. In view of the short-term overcurrent capability of GSCs, the maximum value I_{Gmax} of I_G is set to be 1.3 p.u. in the current limiting. The *P-V* PI controller is designed to achieve the MPPT value P_{Gijref} and generate the AC voltage amplitude v_{fdref}. V_{fdN} is the rated value of v_{fij}, which is added to improve the start-up speed.

The *Q-θ* based reactive power controller contains two operating modes, activated by an enabling signal E_n based on the capacity limit criterion, as shown in (13) and (14). Equation (13) is designated as a primary operating mode. Based on θ_{Gij}, which is positively correlated with the active power output, Q_{Gij} of each WT is allocated adaptively using *Q-θ* droop control. A rational design of droop coefficient k_{Qp} is essential, which is discussed in the subsequent subsection. The first-order inertial loop is added to enhance dynamics and stability with time constant $k_T=0.05$. When E_n changes

from 0 to 1, the reactive power of WTs is set to be the limitation Q_{limit}. Concurrently, the integral loop with gain k_{Qi} in (14) is used to ensure the accurate control of reactive power so that the apparent power of WTij S_{Gij} does not exceed its threshold. Besides, f_G under the proposed control can be maintained at its rated value f_1 if necessary.

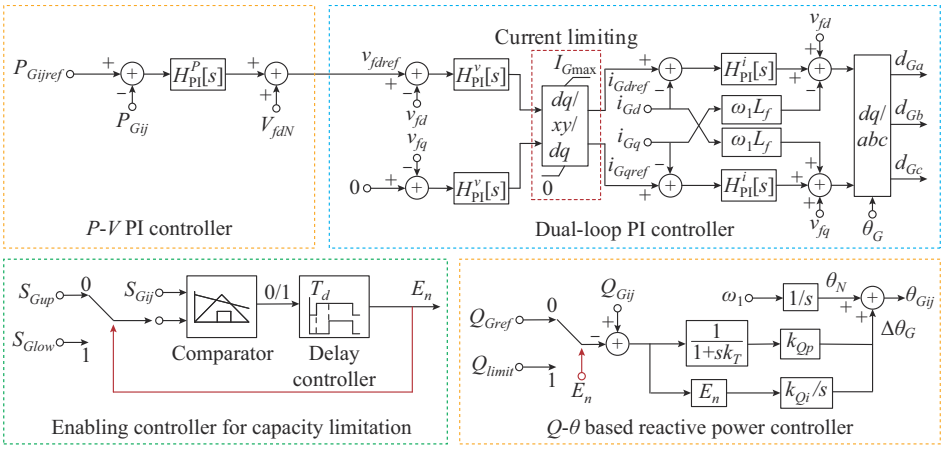

Fig. 5. Diagram of Q-θ type GFM control based on adaptive reactive power allocation for WT GSCs.

$$(Q_{Gij}-Q_{Gref})\frac{k_{Qp}}{1+sk_T}=\theta_{Gij}-\theta_N \tag{13}$$

$$(Q_{Gij}-E_nQ_{limit})\left(\frac{k_{Qp}}{1+sk_T}+E_n\frac{k_{Qi}}{s}\right)=\theta_{Gij}-\theta_N \tag{14}$$

where θ_{Gij} is the voltage angle of WT j at WT string i; and θ_N is the reference voltage angle of each WT generated by a voltage-controlled oscillator. Since Q_{Gij} is adjusted via the change of θ_{Gij}, Q_{Gref} in Q-θ droop control can be set to be 0.

The activation logic of the enabling controller is concisely outlined as follows. When S_{Gij} reaches its upper limit S_{Gup}, the enabling controller is activated and the output of the comparator in Fig. 5 becomes 1, otherwise, it becomes 0. To mitigate maloperation due to transient power disturbances, a delayed judgment is introduced. Combined with the requirement of reactive power support and the overcurrent duration of GSC under AC fault, the delay time is set to be 0.1 s. Only if S_{Gij} is greater than S_{Gup} during the continuous detection time T_d, the delay controller outputs the enabling signal E_n as 1. Moreover, when E_n is 1, S_{Gup} will be switched to the lower limit S_{Glow} of S_{Gij}, functioning as a hysteresis comparator to prevent unnecessary control toggles. Conversely, the enabling controller is deactivated (i.e., $E_n=0$) when S_{Gij} falls below S_{Glow}, resulting in the reset of S_{Glow} to S_{Gup} for subsequent capacity limitation assessments.

In Fig. 5, v_{fd} and v_{fq} are the dq transformation components of v_{fij}; d_{Ga}, d_{Gb}, and d_{Gc} are the three-phase modulation indices of the GSC in WTij; P_{Gij} is the active power generated in WTij; S_{Gij}, P_{Gij}, and Q_{Gij} are calculated based on the terminal voltage v_{Gij} and current i_{Gij} of WTij; $H_{PI}^P[s]$ is the PI transfer function of the active power controller; and $H_{PI}^v[s]$ and $H_{PI}^i[s]$ are the PI transfer functions of the dual-loop voltage and current controllers, respectively. For consistency, all electrical variables in Fig. 5 are expressed in per-unit values.

B. Mechanism of Reactive Power Allocation Among WTs

Take the reactive power allocation among WT strings as an example. For simplicity of analysis, WTi1-WTi10 of WT string i are aggregated as an equivalent WT i. Referring to [24], the inductance of AC collection cables within WT string i is equivalent to L_{Ceqi} based on the reservation of reactive power capacity. Consequently, the power flow dynamics between equivalent WT i and PCC bus can be formulated as:

$$P_{si}=\frac{3V_{si}V_{PCC}}{\omega_1 L_{Ceqi}}\sin(\theta_{si}-\theta_{PCC})\approx\frac{3V_{si}V_{PCC}}{\omega_1 L_{Ceqi}}(\theta_{si}-\theta_{PCC}) \tag{15}$$

$$Q_{si}=\frac{3V_{si}(V_{si}-V_{PCC}\cos(\theta_{si}-\theta_{PCC}))}{\omega_1 L_{Ceqi}}\approx\frac{3V_{si}(V_{si}-V_{PCC})}{\omega_1 L_{Ceqi}} \tag{16}$$

where P_{si} and Q_{si} are the transmitted active and reactive power of equivalent WT i, respectively; θ_{PCC} is the voltage angle of v_{PCC}; and V_{si} and θ_{si} are the RMS values of the phase voltage and angle at the terminal of equivalent WT i, respectively.

Similar to (13), the reactive power output characteristics of equivalent WT i can be written as:

$$\theta_{si}=k_{Qp}(Q_{si}-Q_{Gref})+\theta_N=k_{Qp}Q_{si}+\theta_N \tag{17}$$

Combining (15)-(17), a key relationship between V_{si} and P_{si} is derived as:

$$P_{si}=\frac{3V_{si}V_{PCC}}{\omega_1 L_{Ceqi}}\left[k_{Qp}\frac{3V_{si}(V_{si}-V_{PCC})}{\omega_1 L_{Ceqi}}+\theta_N-\theta_{PCC}\right] \tag{18}$$

Figure 6 illustrates the relationship between V_{si} and P_{si} in (18), taking into account the impact of AC collection cable length (i.e., L_{Ceqi}).

Notably, P_{si} is positively correlated with V_{si}, indicating that equivalent WT i with lower active power output P_{si} will experience smaller terminal voltage V_{si}. Thus, based on (16), these WTs will absorb more reactive power compared to their counterparts with higher P_{si}. Within a reasonable variation range of L_{Ceqi}, the impact on V_{si} is minimal, suggesting that the reactive power outputs of WTs with the same active power level are basically equal.

As shown in Fig. 4, WT GSCs act to absorb reactive power over a wide active power range during normal operation. This naturally aligns with the Q-θ droop control, which adap-

tively assigns higher reactive power absorption responsibilities to WTs with lower active power output. In abnormal scenarios where AFBs cannot be switched off, the increased surplus reactive power within the AC collection network can also be largely absorbed by WTs with lower active power output. The overload risk of WTs with higher active power output is mitigated.

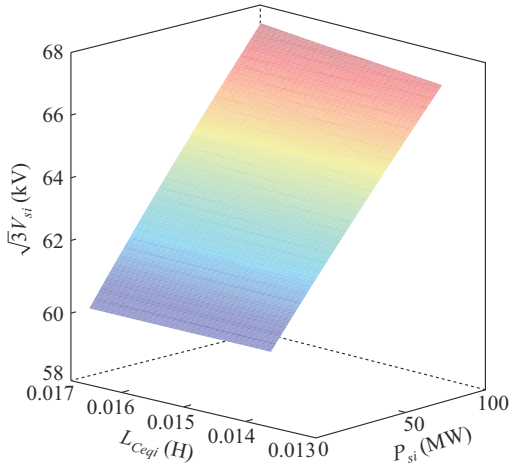

Fig. 6. Relationship between V_{si} and P_{si} in (18).

Under abnormal conditions where AFBs are not available, WTs with higher active power output are forced to provide the reactive power for DRs, as evident from Fig. 4. To prevent the overload risk of WTs with higher active power output, a switch from reactive power droop control to PI control is adopted for WTs when E_n is activated. The upper limit S_{Gup} is set to be 1.01 p.u., taking into account the small spare capacity retained by WTs. Hence, to maximize the utilization of the capacity margin, Q_{limit} in (14) can be set to be 0.1 p.u. or −0.1 p.u. depending on whether Q_{Gij} is greater or less than 0 at the previous sampling time. When the wind power of WTs is reduced to S_{Glow}, E_n becomes 0, and the reactive power PI control is disabled. Since the maximum reactive power output of WTs is about 0.3 p.u., the lower limit S_{Glow} in the hysteresis comparator can be selected as 0.96 p.u.. In this way, frequent triggering of the enabling controller can be prevented.

C. Design of Droop Coefficient k_{Qp}

Combined with (15), the voltage angle difference between equivalent WTs 1 and 2 is further written in (19), where the length of AC collection cables is nearly the same.

$$(\theta_{s1}-\theta_{PCC})-(\theta_{s2}-\theta_{PCC})=\frac{\omega_1 L_{Ceq1}}{3V_{s1}V_{PCC}}\left(P_{s1}-\frac{P_{s2}V_{s1}}{V_{s2}}\right) \quad (19)$$

Based on (17), the relationship between the voltage angle and reactive power of equivalent WTs 1 and 2 is expressed as:

$$\theta_{s1}-\theta_{s2}=k_{Qp}(Q_{s1}-Q_{s2}) \quad (20)$$

As shown in (19), the voltage angle difference between equivalent WTs 1 and 2 is mainly determined by their active power output, ignoring the slight effect of voltage magnitude. When the active power output of WTs is determined, the voltage angle difference between θ_{s1} and θ_{s2} can be constant. Hence, their reactive power difference in (20) will be inversely proportional to the droop coefficient k_{Qp}. Thus, k_{Qp} is the key factor in the reactive power allocation among WTs. Substituting (19) into (20), the relationship between active and reactive power of equivalent WTs 1 and 2 can be obtained as:

$$k_{Qp}(Q_{s1}-Q_{s2})=\frac{\omega_1 L_{Ceq1}}{3V_{s1}V_{PCC}}\left(P_{s1}-\frac{P_{s2}V_{s1}}{V_{s2}}\right) \quad (21)$$

As k_{Qp} in (21) is less than $\omega_1 L_{Ceq1}/(3V_{s1}V_{PCC})$, the reactive power difference will be greater than the active power difference, ignoring the slight dissimilarities of V_{s1} and V_{s2}. This will cause the WTs with higher active power output to generate excess reactive power during normal operation, imposing WTs with lower active power output to absorb additional reactive power. Hence, k_{Qp} cannot be selected too small. The objective of the lower limit of k_{Qp} is to maintain the reactive power output of WTs operating at the rated active power output essentially unchanged under wind power fluctuations of OWFs.

Assume that all equivalent WTs are operating at their rated capacity. At a given time, the active power output of equivalent WT 1 is slightly reduced by ΔP_{s1}. Based on (21), the reactive power fluctuations of equivalent WTs 1 and 2 can be expressed in (22) regardless of the slight variation of voltage variables.

$$k_{Qp}(\Delta Q_{s1}-\Delta Q_{s2})=\frac{\omega_1 L_{Ceq1}}{3V_{s1}V_{PCC}}\Delta P_{s1} \quad (22)$$

where ΔQ_{si} and ΔP_{si} are the variation of transmitted reactive power and active power of equivalent WT i, respectively.

Based on (3), the variation of Q_{DR} is written as:

$$\Delta Q_{DR}=\Delta P_{s1}\tan\varphi\approx\Delta Q_{s1}+\sum_{i=2}^{10}\Delta Q_{si} \quad (23)$$

To determine the lower limit $k_{Qp,\min}$ of k_{Qp}, ΔQ_{s2}-ΔQ_{s10} are ideally set to be 0. Thus, combining (22) with (23), $k_{Qp,\min}$ can be obtained as:

$$k_{Qp,\min}=\frac{\omega_1 L_{Ceq1}}{3V_{s1}V_{PCC}}\frac{1}{\tan\varphi_{\max}}\approx 0.25 \quad (24)$$

where $\varphi_{\max}$ is the maximum power factor angle of DRs operating at rated active power output ($\tan\varphi_{\max}\approx 0.4$).

Additionally, it is not advisable to set k_{Qp} too large. For example, assume that k_{Qp} in (21) is 50 times $\omega_1 L_{Ceq1}/(3V_{s1}V_{PCC})$, i.e., $k_{Qp}\approx 5$. When the difference of active power output between WTs is at its maximum of 1 p.u., the reactive power deviation is only about 0.02 p.u.. This will not only impede WTs with lower active power output from contributing more reactive power, but also result in poor dynamic response. Hence, k_{Qp} is set to be 0.75 in this paper.

IV. Sequence Impedance Modeling of Wind Farms Under Different GFM Controls

The sequence impedance models of the DR-HVDC system for OWF integration comprise two parts: DR-HVDC and wind farms. The impedance model of DRs $\boldsymbol{Z}_{PN}^{DR}$ has been established in [25]. Therefore, this section mainly focuses on

the modeling of wind farms under different GFM controls.

A. Modeling of Wind Farms Under Proposed Q-θ Type GFM Control

The equivalent circuit of WT string i is established in Fig. SA1 of Supplementary Material A. Referring to [25], Δ is a small-signal form. The variables in bold represent their vector forms in the frequency domain within a ±3-order harmonic frequency range. As depicted in Fig. 2, the dynamic equation of GSC in WTi1 is derived via a small-signal representation:

$$\Delta \boldsymbol{v}_{fi1} = 0.5 V_{dcG} \Delta \boldsymbol{d}_{Gi1} - \boldsymbol{Z}_{Lf}^{p} \Delta \boldsymbol{i}_{Gi1} \tag{25}$$

where $\Delta \boldsymbol{v}_{fi1}$, $\Delta \boldsymbol{d}_{Gi1}$, and $\Delta \boldsymbol{i}_{Gi1}$ are the small-signal vector forms of phase voltage v_{fi1}, modulation index d_{Gi1}, and current i_{Gi1} in the GSC of WTi1, respectively; V_{dcG} is the rated DC voltage of GSC; and $\boldsymbol{Z}_{Lf}^{p}$ is the harmonic impedance matrix of L_f.

Based on the architecture of the proposed Q-θ type GFM control in Fig. 5, $\Delta \boldsymbol{d}_{Gi1}$ is written in (26), considering the frequency coupling caused by asymmetric control in dq axis.

$$\Delta \boldsymbol{d}_{Gi1} = (\boldsymbol{I} - \boldsymbol{G}_{Hv}) \Delta \boldsymbol{v}_{fi1} - \boldsymbol{G}_{Hi} \Delta \boldsymbol{i}_{Gi1} - \boldsymbol{G}_{HP} \Delta \boldsymbol{P}_{Gi1} + \boldsymbol{G}_{H\theta} \Delta \boldsymbol{\theta}_{Gi1} \tag{26}$$

where $\Delta \boldsymbol{P}_{Gi1}$ and $\Delta \boldsymbol{\theta}_{Gi1}$ are the small-signal vector forms of P_{Gi1} and θ_{Gi1}, respectively; $\boldsymbol{I}$ is the unit matrix; $\boldsymbol{G}_{Hv}$, $\boldsymbol{G}_{Hi}$, and $\boldsymbol{G}_{HP}$ are the transfer function matrices decided by the dual-loop PI controller, the current PI controller, and the active power PI controller, respectively [26]; and the transfer function matrix $\boldsymbol{G}_{H\theta}$ reflects the disturbance of θ_{Gi1} to dq transformation.

$\Delta \boldsymbol{P}_{Gi1}$ and $\Delta \boldsymbol{\theta}_{Gi1}$ can be expressed as follows. Considering that E_n is basically not activated under normal operation, it has been omitted from subsequent equations.

$$\Delta \boldsymbol{P}_{Gi1} = 3(\boldsymbol{T}[v_{Gi1}] \Delta \boldsymbol{i}_{Gi1} + \boldsymbol{T}[i_{Gi1}] \Delta \boldsymbol{v}_{Gi1}) \tag{27}$$

$$\Delta \boldsymbol{\theta}_{Gi1} = \left(\frac{k_{Qp}}{1 + s k_T} + \frac{k_{Qi}}{s} E_n \right) \Delta \boldsymbol{Q}_{Gi1} \quad s = \mathrm{j} 2\pi (f_p - f_1) \tag{28}$$

$$\Delta \boldsymbol{v}_{Gi1} = \Delta \boldsymbol{v}_{fi1} + \boldsymbol{Z}_{Lf}^{p} \Delta \boldsymbol{i}_{Gi1} \tag{29}$$

$$\Delta \boldsymbol{Q}_{Gi1} = 3(\boldsymbol{T}[v_{Gi1} \mathrm{e}^{-\mathrm{j}\pi/2}] \Delta \boldsymbol{i}_{Gi1} + \boldsymbol{T}[i_{Gi1} \mathrm{e}^{\mathrm{j}\pi/2}] \Delta \boldsymbol{v}_{Gi1}) \tag{30}$$

where $\boldsymbol{T}[\cdot]$ is the Toeplitz matrix defined for convolution operations in the frequency domain; $\Delta \boldsymbol{v}_{Gi1}$ is the small-signal vector form of terminal voltage v_{Gi1} in WTi1; $\Delta \boldsymbol{Q}_{Gi1}$ is the small-signal vector form of Q_{Gi1}; and f_p is the frequency of the additional positive-sequence small-signal voltage.

Substituting (27) - (30) into (26), the analytical model of the proposed Q-θ type GFM control can be expressed as:

$$\Delta \boldsymbol{d}_{Gi1} = \boldsymbol{H}_v \Delta \boldsymbol{v}_{fi1} + \boldsymbol{H}_i \Delta \boldsymbol{i}_{Gi1} \tag{31}$$

$$\boldsymbol{H}_v = \boldsymbol{I} - \boldsymbol{G}_{Hv} - 3\boldsymbol{G}_{HP} \boldsymbol{T}[i_{Gi1}] + 3\boldsymbol{G}_{H\theta} \frac{k_{Qp}}{1 + s k_T} \boldsymbol{T}[i_{Gi1} \mathrm{e}^{\mathrm{j}\pi/2}] \tag{32}$$

$$\boldsymbol{H}_i = -\boldsymbol{G}_{Hi} - 3\boldsymbol{G}_{HP} (\boldsymbol{T}[v_{Gi1}] + \boldsymbol{T}[i_{Gi1}] \boldsymbol{Z}_{Lf}^{p}) + 3\boldsymbol{G}_{H\theta} \frac{k_{Qp}}{1 + s k_T} (\boldsymbol{T}[v_{Gi1} \mathrm{e}^{-\mathrm{j}\pi/2}] + \boldsymbol{T}[i_{Gi1} \mathrm{e}^{\mathrm{j}\pi/2}] \boldsymbol{Z}_{Lf}^{p}) \tag{33}$$

In conclusion, combining (25) with (31), the relationship between the AC current and voltage of GSC in WTi1 can be derived in (34). Thus, the sequence impedance model of WTi1 $\boldsymbol{Z}_{PN}^{WT}$ containing the impedance of its AC step-up transformer is derived in (35). Moreover, according to the series and parallel structure of WTij and WT string i in Fig. 2, the sequence impedance model of wind farms $\boldsymbol{Z}_{PN}^{WF}$ can be derived.

$$\Delta \boldsymbol{v}_{fi1} = \underbrace{(\boldsymbol{I} - 0.5 V_{dcG} \boldsymbol{H}_v)^{-1} (-0.5 V_{dcG} \boldsymbol{H}_i + \boldsymbol{Z}_{Lf}^{p})}_{\boldsymbol{Z}^{G}} (-\Delta \boldsymbol{i}_{Gi1}) \tag{34}$$

$$\boldsymbol{Z}_{PN}^{WT} = \begin{bmatrix} Z_{pp}^{WT} & Z_{pn}^{WT} \\ Z_{np}^{WT} & Z_{nn}^{WT} \end{bmatrix} = \begin{bmatrix} \boldsymbol{Z}^{G}(4,4) & \boldsymbol{Z}^{G}(4,2) \\ \boldsymbol{Z}^{G}(2,4) & \boldsymbol{Z}^{G}(2,2) \end{bmatrix} // \boldsymbol{Z}_{PN}^{Cf} + \boldsymbol{Z}_{PN}^{LT} \tag{35}$$

where Z_{pp}^{WT} and Z_{nn}^{WT} are the positive- and negative-sequence impedances, respectively, while their frequency-coupling terms are Z_{pn}^{WT} and Z_{np}^{WT}; $\boldsymbol{Z}_{PN}^{Cf}$ and $\boldsymbol{Z}_{PN}^{LT}$ are the sequence impedances of C_f and L_T, respectively; and // represents the relationship of impedances connected in parallel.

B. Modeling of WTs Under Q-f Type GFM Control and Distributed PLL Type GFM Control

As proposed in [16], the small-signal model of the Q-f type GFM control can be expressed in (36). Similarly, replacing (36) with (28), the sequence impedance model of wind farms under Q-f type GFM control can be obtained.

$$\Delta \boldsymbol{\theta}_{Gi1} = k_Q \Delta \boldsymbol{Q}_{Gi1} \frac{1}{s} \tag{36}$$

It is observed that the difference between (28) and (36) is mainly attributed to an extra term $1/s$ in the Q-f type GFM control. Thus, the effects of $\Delta \boldsymbol{Q}_{Gi1}$ at medium- and high-frequency bands will be weakened. Conversely, the impedance characteristics at the rated frequency range are amplified.

In comparison to the above two GFM controls, the distributed PLL type GFM control in [14] contains additional effects resulting from the PLL-based frequency controller and PLL disturbance. Figure 7 presents the structure of the PLL-based frequency controller, where v_{fqref} and θ_{fi1} are the reference value of the q-axis voltage v_{fq} and the angle tracked by PLL of v_{fi1}, respectively; ω_{Gi1} is the angular frequency of v_{PCC}; ω_{Gref} is the reference angular frequency of ω_{Gi1}; k_ω is the droop coefficient of the frequency controller; and k_{lp} and k_{li} are the proportional and integral parameters of the PI controller of PLL, respectively.

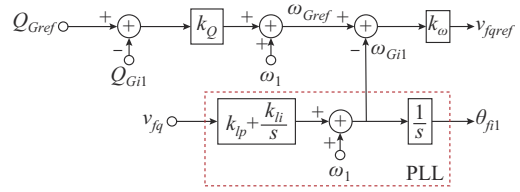

Fig. 7. PLL-based frequency controller of distributed PLL type GFM control.

The added small-signal model $\Delta \boldsymbol{d}_{Gi1,PLL}$ can be written as:

$$\Delta \boldsymbol{d}_{Gi1,PLL} = \boldsymbol{G}_{Hv} \Delta \boldsymbol{v}_{fqref} + \boldsymbol{G}_{HPLL} \Delta \boldsymbol{\theta}_{fi1} \tag{37}$$

where $\Delta \boldsymbol{v}_{fqref}$ and $\Delta \boldsymbol{\theta}_{fi1}$ are the small-signal vector forms of v_{fqref} and θ_{fi1}, respectively; and $\boldsymbol{G}_{HPLL}$ is the transfer function matrix decided by the disturbance of PLL in dq transformation.

The small-signal models for $\Delta \boldsymbol{\theta}_{fi1}$ and $\Delta \boldsymbol{v}_{fqref}$ can be further expressed in (38) and (39). It is noted that the disturbance of

PLL in (38) tends to diminish the damping characteristics of the GSC near f_1 [27]. Furthermore, the PLL-based frequency controller in Fig. 7 is employed to obtain v_{fqref} by controlling v_{fq}. Consequently, an additional control delay T_c in (39) is introduced, which may result in an elevated risk of high-frequency oscillations.

$$\Delta\boldsymbol{\theta}_{fi1}=H_{PLL}[s]\Delta\boldsymbol{v}_{fq}=H_{PLL}[s]\boldsymbol{T}_{v4}\Delta\boldsymbol{v}_{fi1} \tag{38}$$

$$\Delta\boldsymbol{v}_{fqref}=k_{\omega}(\Delta\boldsymbol{\omega}_{Gref}+s\Delta\boldsymbol{\theta}_{fi1})= k_{\omega}(k_{Q}\Delta\boldsymbol{Q}_{Gi1}+s\mathrm{e}^{-sT_c}H_{PLL}[s]\Delta\boldsymbol{v}_{fq}) \tag{39}$$

where $H_{PLL}[s]$ is the transfer function of PLL; $\Delta\boldsymbol{v}_{fq}$ is the small-signal vector form of v_{fq}; $\boldsymbol{T}_{v4}$ is the conversion gain matrix from $\Delta\boldsymbol{v}_{fq}$ to $\Delta\boldsymbol{v}_{fi1}$, which can be referred to [25]; and $\Delta\boldsymbol{\omega}_{Gref}$ is the small-signal vector form of ω_{Gref}. Substituting (37) into (25), the sequence impedance model of wind farms under distributed PLL type GFM control can be obtained.

V. Simulation Verification

To verify the feasibility of the proposed control, a ±320 kV/1000 MW DR-HVDC system shown in Fig. 1 is established in PSCAD/EMTDC. The WT string 1 comprises 10 × 10 MW WTs connected in parallel. To enhance simulation efficiency, WT strings 2-5 and 6-10 are aggregated into the 400 MW WT_2 and 500 MW WT_3, respectively [15]. The electrical parameters of the system are presented in Table I, and the control parameters of WTs under different GFM controls are listed in Table II.

TABLE II
Parameters of WTs Under Different GFM Controls

Component	Parameter	Value
GFM control	Proportional and integral parameters of AC current controller	$k_{pi}=0.5$, $k_{ii}=50$
	Proportional and integral parameters of AC voltage controller	$k_{pv}=1$, $k_{iv}=100$
	Proportional and integral parameters of active power controller	$k_{pP}=5$, $k_{iP}=100$
Proposed *Q-θ* type GFM control	Proportional and integral parameters of reactive power controller	$k_{Qp}=0.75$, $k_{Qi}=20$
Q-f type GFM control	Proportional parameter of reactive power controller	$k_Q=5$
Distributed PLL type GFM control	Proportional parameters of reactive power controller and frequency controller	$k_Q=5$, $k_\omega=0.2$
	Proportional and integral parameters of PI controller of PLL	$k_{lp}=0.1$, $k_{li}=0.4$

A. Validation of Proposed Q-θ Type GFM Control

1) Scenario 1: Normal Conditions

To test the adaptive capability of the proposed control across a wide power range, the wind power is adjusted as follows. OWFs operate in grid-connected mode at 2 s, where the active power of WT11-WT110 at WT string 1 is 1 p.u.. WT_2 and WT_3 are in the initial stages of power generation. During 2-16 s, P_{G11}-P_{G15} remain unchanged, and P_{G16}-P_{G110} decrease by 0.05 p.u. at 8 s. WT11-WT110 are used to simulate some WTs with higher active power output in OWFs. The wind power of WT_2 and WT_3 fluctuates disorderly, representing the majority of WTs. Figure 8 presents the simulation results of wind power fluctuations in OWFs under the proposed control, while the simulation results under the conventional GFM control are basically the same as those in Fig. 8 and will not be given again.

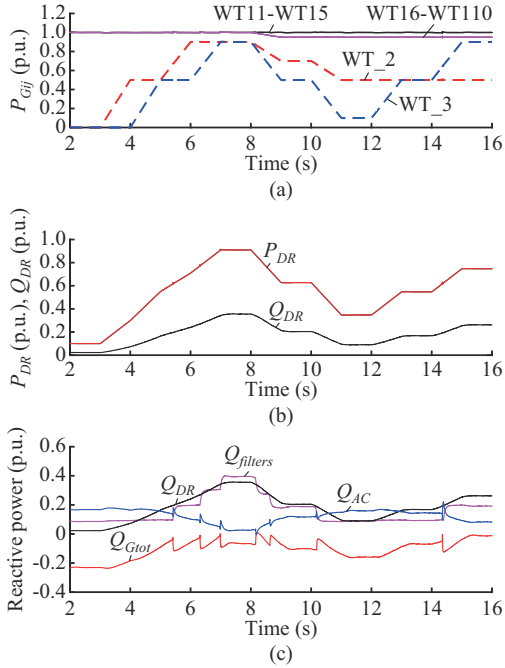

Fig. 8. Simulation results of wind power fluctuations in OWFs under proposed control. (a) Active power of WTs. (b) Active and reactive power of DRs. (c) Reactive power response characteristics of DRs, AFBs, AC collection networks, and WTs.

It can be observed in Fig. 8(a) that WTs can smoothly transmit wind power. As shown in Fig. 8(b), the absorbed reactive power of DRs Q_{DR} correlates positively with its transmitted active power P_{DR}. The reactive power response characteristics of DRs, AFBs, AC collection networks, and WTs are depicted in Fig. 8(c). Based on the reactive power demand of DRs, the AFB can be switched on or off to regulate its output reactive power $Q_{filters}$. The AC collection networks present reactive capacitance characteristics within a wide power range. In this case, WTs are required to absorb the surplus reactive power of Q_{AC} and $Q_{filters}$.

Figure 9 illustrates the comparisons of simulation results of wind power fluctuations under the proposed control and the conventional GFM control (considering that the results of *Q-f* type GFM and distributed PLL type GFM controls are similar, the *Q-f* type GFM control is taken as an example).

It is indicated in Fig. 9(a) that the reactive power absorbed by WT11-WT110, WT_2, and WT_3 is positively correlated with their active power output. The reactive power of WT11-WT110 exhibits minimal variations even under the large wind power fluctuations of OWFs, which effectively mitigates the overload risk of WTs. Besides, the reactive power allocated to WT11-WT15 at the end of WT string 1 is slightly less than that of WT16-WT110 at the head end. Hence, the reactive power can be allocated adaptively based

on the actual active power output of WTs, which is consistent with the analysis in Section III.

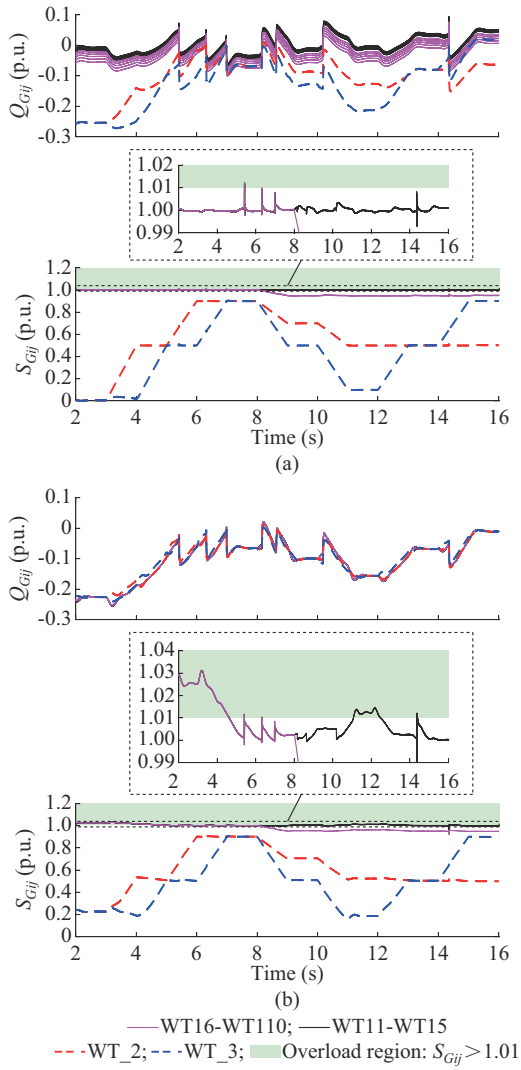

Fig. 9. Comparisons of simulation results of wind power fluctuations under different GFM controls. (a) Reactive and apparent power of WTs under proposed control. (b) Reactive and apparent power of WTs under *Q-f* type GFM control.

However, in Fig. 9(b), Q_{Gtot} is allocated evenly among WTs, which introduces an overload risk of WT11-WT110 in numerous operating cases, particularly during low active power output periods of OWFs, such as during the start-up phase. As shown in Fig. SA2(a) and (b) of Supplementary Material A, the AC currents of WT GSCs under the proposed control can also be maintained in a reasonable range, while those under the *Q-f* type GFM control are susceptible to the risk of overcurrent. DC voltages of WTs under the above two GFM controls can be maintained at a stable level.

2) Scenario 2: AFB Maloperation Conditions

The simulation setup for wind power fluctuations under AFB maloperation conditions is the same as that in Fig. 8(a). As depicted in Fig. 10, with the increase of wind power during 2-8 s, it is not possible for AC filters to increase the number of AFBs to meet the reactive power demand of DRs. It was not until 8 s that three AFBs responded and were put into operation; however, they subsequently could not be switched off in accordance with the required reactive power demand. Thus, it can be observed that WTs passively absorb or generate more reactive power Q_{Gtot} than that shown in Fig. 8(c).

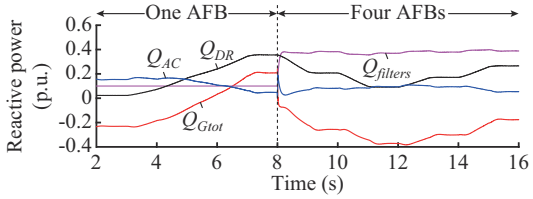

Fig. 10. Reactive power response characteristics of DRs, AFBs, AC collection networks, and WTs under AFB maloperation conditions.

Figure 11 shows the simulation results of reactive power allocation of WTs under AFB maloperation conditions. As Fig. 11(a) indicates, the reactive power of WTs is positively correlated with their active power output. WT_2 and WT_3 can adaptively bear more reactive power. When the apparent power S_{Gij} of WT11-WT110 reaches the threshold S_{Gup} after about 6.5-6.6 s, E_n is automatically activated, as shown in Fig. SA3 of Supplementary Material A. The reactive power Q_{Gij} of WT11-WT110 can be accurately controlled as Q_{limit}. Besides, when the wind power of WT16-WT110 decreases after 8 s, E_n can be deactivated when S_G is lower than S_{Glow}, allowing WT_2 and WT_3 to participate in reactive power allocation again. As shown in Fig. 11(c), AC currents of WT GSCs are maintained in a reasonable range. Consequently, even under AFB maloperation conditions, each WT can operate normally without overloading. However, compared with Fig. 9(b), Fig. 11(b) indicates that the risk of exceeding the capacity limit S_{Gup} increases for WTs with higher active power output under the *Q-f* type GFM control. Besides, the AC currents of WT GSCs significantly exceed the limit under the *Q-f* type GFM control, as shown in Fig. 11(d).

Thus, the proposed *Q-θ* type GFM control based on adaptive reactive power allocation is an effective scheme for ensuring the safe operation of OWFs.

B. Simulation of an AC Fault Occurring on WT Side

Since the fault ride-through capability of DR-HVDC systems is fully evaluated under an offshore fault at the PCC bus and an onshore fault [12], [16], this paper focuses on the analysis of an AC fault occurring on the WT side.

When an AC fault occurs on the WT110 side shown in Fig. 2, V_{PCC} drops and a large amount of reactive power needs to be absorbed at the fault point, resulting in a notable reduction in the active power of the functional WT strings. To maximize the wind power transmission, an AC fault control mode of AFBs is designed for full operation during the above AC fault, where all AFBs do not follow the conventional active power threshold based switching logic.

Figure 12 depicts the simulation results of a three-phase solid short-circuit fault occurring at the head end of WT110 at 7 s.

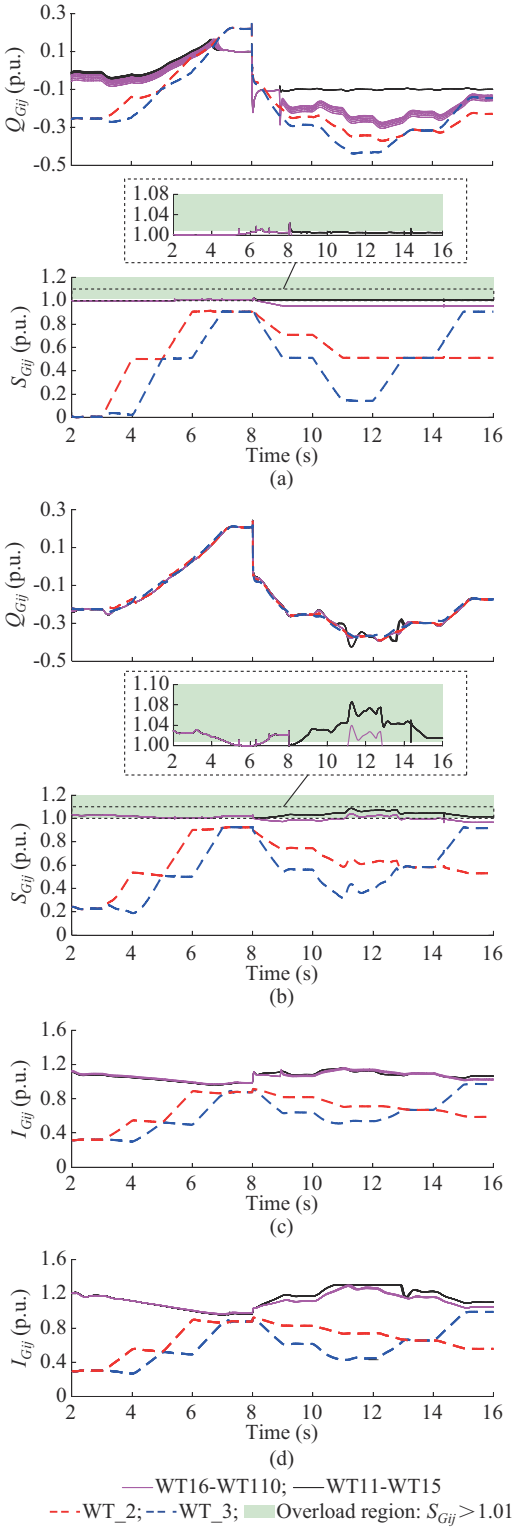

Fig. 11. Comparisons of simulation results under AFB maloperation conditions. (a) Reactive and apparent power of WTs under proposed control. (b) Reactive and apparent power of WTs under *Q-f* type GFM control. (c) AC currents of WTs under proposed control. (d) AC currents of WTs under *Q-f* type GFM control.

After 0.1 s, the AC breaker is triggered to disconnect WT string 1. The wind power fluctuations are the same as those in Fig. 8(a). In this case, the DC voltages and AC currents of WTs are similar under *Q-f* type GFM control and proposed control. For space-saving, the proposed control is taken as an example, and the results are shown in Fig. 12(a). It can be observed that the DC voltages of WT11-WT110 increase rapidly to the upper limits as the AC fault occurs.

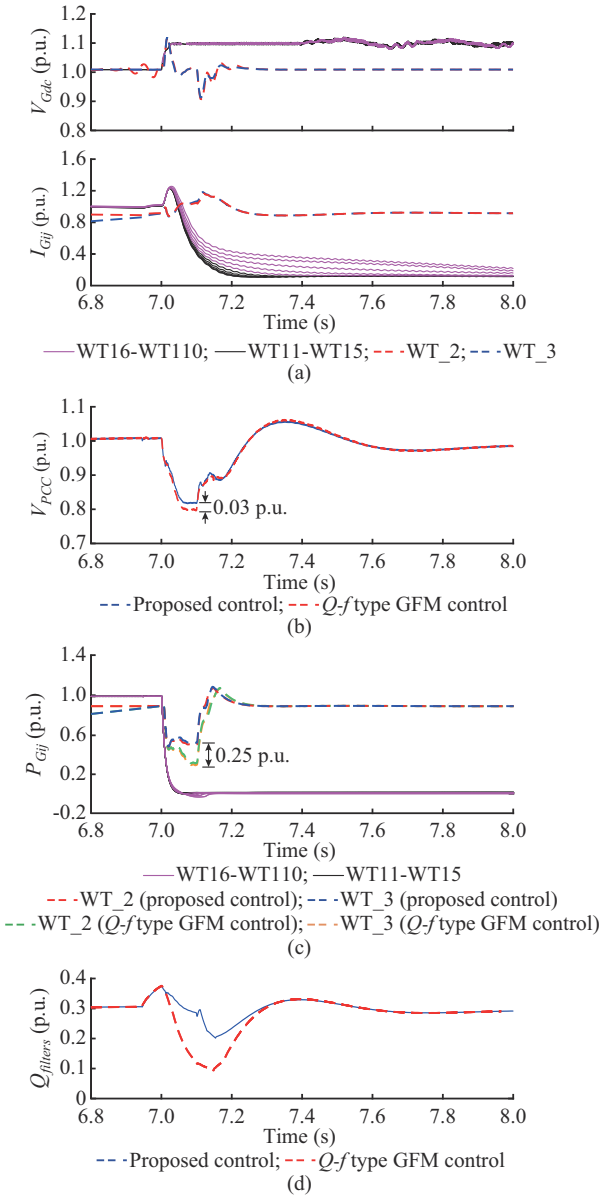

Fig. 12. Simulation results of a three-phase solid short-circuit fault occurring at head end of WT110. (a) DC voltages and AC currents of WTs under proposed control. (b) AC voltage at PCC under different GFM controls. (c) Active power of WTs under different GFM controls. (d) Reactive power of AC filters under different GFM controls.

The AC currents of WT11-WT110 will rise temporarily, which can be suppressed quickly by the fault ride-through control of the WTs. While WT_2 and WT_3 can maintain the DC voltages and AC currents within the normal range after a transient shock. As Fig. 12(b) and (c) shows, AC voltage V_{PCC} and active power of WT_2 and WT_3 drop sharply due to the clamping of the fault point voltage, while the active power of WT11-WT110 in the event of the AC fault is reduced to 0. In Fig. 12(d), following the conventional switching logic of AFBs under *Q-f* type GFM control will re-

sult in a reduction in $Q_{filters}$. However, by activating the AC fault control mode under the proposed control, 4 AFBs can be activated to compensate for the reactive power at the fault point. Thus, V_{PCC} can be effectively increased by about 0.03 p.u., as illustrated in Fig. 12(b). The active power output of WT_2 and WT_3 is enhanced by about 0.25 p.u., ensuring the maximized sustained active power transmission of the DR-HVDC system.

C. Stability Analysis of DR-HVDC System Under Different GFM Controls

The validation of the sequence impedance model $\boldsymbol{Z}_{PN}^{WF}$ under the proposed control is shown in Fig. SA4 of Supplementary Material A. It can be observed that the simulation results of $\boldsymbol{Z}_{PN}^{WF}$ in the red circles match well with their analytical results in the blue line, validating the correctness of established models. It is noted that the frequency-coupling terms Z_{pn}^{WF} and Z_{np}^{WF} have negligible impedance amplitudes in the high-frequency bands above 1.5 kHz, so there is an allowable measurement error.

Considering that dual-loop and active power PI controllers are common components in the proposed control, *Q-f* type GFM control and distributed PLL type GFM control, this paper mainly analyzes the impacts of various reactive power controllers on system stability. Referring to [25], equivalent positive-sequence impedances of DR-HVDC and OWFs are denoted as $Z_{PP,SISO}^{DR}$ and $Z_{PP,SISO}^{WF}$. Figure 13 presents $Z_{PP,SISO}^{DR}$ and $Z_{PP,SISO}^{WF}$ under the proposed control with varying k_{Qp}, where the WTs operate under rated power operating conditions. It can be observed that the reactive power controller primarily affects $Z_{PN,SISO}^{WF}$ at around 50 Hz. As k_{Qp} increases, the negative damping will be introduced, resulting in a reduction of phase margin. Notwithstanding, the system exhibits robust stability characteristics within the range of k_{Qp} designed in Section III. Since the impact of integral gain k_{Qi} on $Z_{PN,SISO}^{WF}$ is negligible, it is no longer described.

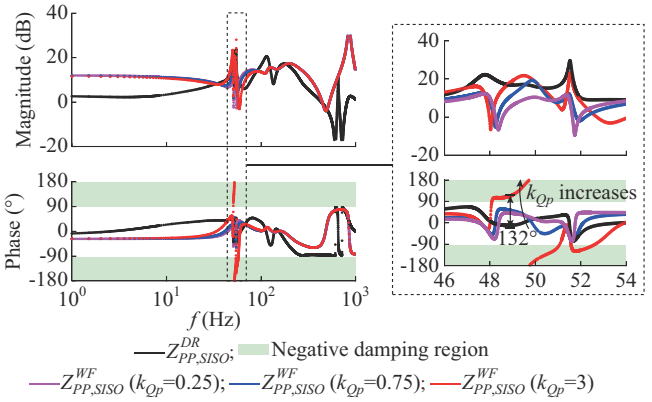

Fig. 13. Equivalent sequence impedances of DR-HVDC and OWFs under proposed control with different k_{Qp}.

Figure 14 depicts $Z_{PP,SISO}^{DR}$ and $Z_{PP,SISO}^{WF}$ under the *Q-f* type GFM control with varying k_Q. Compared with the proposed control, a phase jump is more likely to occur at around 50 Hz. Increasing k_Q by a large amount will introduce negative damping, similar to that under the proposed control. Thus, it is advisable to maintain a relatively low k_Q while ensuring that the dynamic response requirements of the reactive power are met. The impact of k_Q under distributed PLL type GFM control on $Z_{PP,SISO}^{WF}$ is similar to that of the other two GFM controls, and the system can remain stable across a wide range of k_Q.

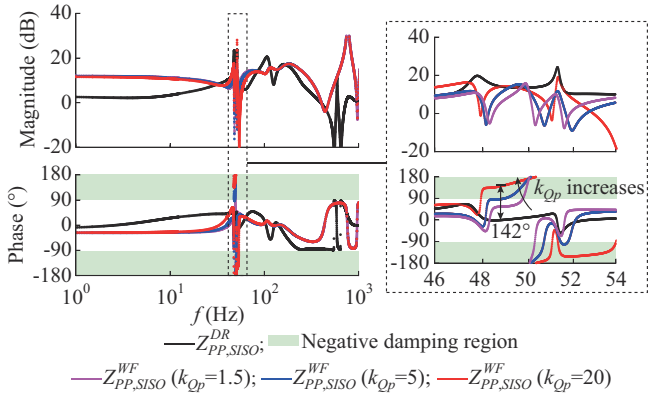

Fig. 14. Equivalent sequence impedances of DR-HVDC and OWFs under *Q-f* type GFM control with different k_Q.

Figure 15 illustrates $Z_{PP,SISO}^{DR}$ and $Z_{PP,SISO}^{WF}$ under distributed PLL type GFM control with different k_ω when the control delay T_c is set to be 50 μs. It is evident that the PLL-based frequency controller has a notable impact on various frequency bands of $Z_{PP,SISO}^{WF}$. Especially, as k_ω increases to 0.46, a high-frequency oscillation emerges at about 1130 Hz, attributable to negative damping caused by the additional control delay in Fig. 7. Besides, as shown in (39), both the integral coefficient k_{lp} of PI controller of PLL and T_c directly affect the above resonant risk through the PLL-based frequency controller. Hence, k_ω should be relatively small to mitigate the impact of the PLL-based frequency controller.

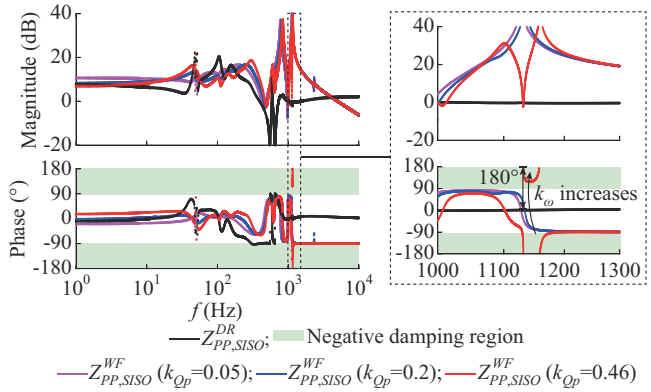

Fig. 15. Equivalent sequence impedances of DR-HVDC and OWFs under distributed PLL type GFM control with different k_ω.

Figure 16 presents the time-domain simulation results when k_ω is increased from 0.2 to 0.46 at 7 s. It can be observed in Fig. 16(a) that v_{PCC} becomes unstable after 7 s. Combined with the fast Fourier transform (FFT) analysis, the resonance frequency of v_{PCC} with its coupling frequency can be consistent with the analytical results in Fig. 15.

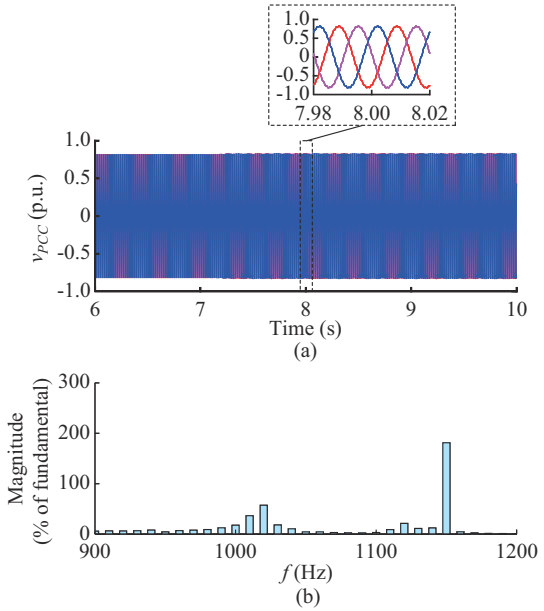

Fig. 16. Time-domain simulation results when k_ω is increased from 0.2 to 0.46 at 7 s. (a) Waveforms of v_{PCC}. (b) FFT of v_{PCC} when k_ω=0.46 (fundamental is 10 Hz).

VI. Conclusion

This paper proposes a Q-θ type GFM control based on adaptive reactive power allocation for OWFs connected to a DR-HVDC system. The active power controller of WTs coordinates the AC voltage amplitude at the PCC bus, while the reactive power controller automatically allocates reactive power according to the voltage angle difference among WTs. The capacity of WTs with lower active power output can be optimally utilized, thereby allowing WTs with higher active power output to absorb less reactive power.

Together with the enabling controller for capacity limitation, the proposed control prevents the overload risk of WT GSCs without increasing their rated capacity, and even reserves capacity for other critical needs such as frequency support for the onshore grid.

The effectiveness of the proposed control is demonstrated under normal conditions and AFB maloperation conditions by comparing it with Q-f type GFM controls. In addition, the DR-HVDC system can continue to transmit most of the active power under an AC fault on the WT side by adopting the AC fault control scheme for AFBs. Based on the established impedance models under three GFM controls, it is indicated that the corresponding three types of reactive power controllers are not conducive to improving system stability, due to the potential introduction of negative damping around 50 Hz. Therefore, it is recommended to select a relatively small reactive power droop coefficient. Nevertheless, the DR-HVDC systems still show favorable stability characteristics. Furthermore, the stability analysis suggests that the distributed PLL-type GFM control may introduce high-frequency oscillations due to the additional control delay in the PLL-based frequency controller.

References

[1] H. Zhang, W. Xiang, W. Lin *et al*., "Grid forming converters in renewable energy sources dominated power grid: control strategy, stability, application, and challenges," *Journal of Modern Power Systems and Clean Energy*, vol. 9, no. 6, pp. 1239-1256, Nov. 2021.

[2] H. Lin, T. Xue, J. Lyu *et al*., "Impact of different AC voltage control modes of wind-farm-side MMC on stability of MMC-HVDC with offshore wind farms," *Journal of Modern Power Systems and Clean Energy*, vol. 11, no. 5, pp. 1687-1699, Sept. 2023.

[3] W. Xiang, W. Yuan, L. Xu *et al*., "DC fault study of a point-to-point HVDC system integrating offshore wind farm using high-temperature superconductor DC cables," *IEEE Transactions on Energy Conversion*, vol. 37, no. 1, pp. 377-388, Mar. 2022.

[4] P. Meng, W. Xiang, Y. He *et al*., "Coordination control of wind farm integrated cascaded hybrid HVDC system in weak grids," *IEEE Transactions on Power Delivery*, vol. 38, no. 3, pp. 1837-1847, Jun. 2023.

[5] A. Nami, J. L. Rodriguez-Amenedo, S. Arnaltes *et al*., "Frequency control of offshore wind farm with diode-rectifier-based HVDC connection," *IEEE Transactions on Energy Conversion*, vol. 35, no. 1, pp. 130-138, Mar. 2020.

[6] W. Xiang, M. Yang, and J. Wen, "DR-MMC hub based hybrid AC/DC collection and HVDC transmission system for large-scale offshore wind farms," *Journal of Modern Power Systems and Clean Energy*. DOI: 10.35833/MPCE.2024.000229

[7] R. Li, L. Yu, and L. Xu, "Offshore AC fault protection of diode rectifier unit-based HVDC system for wind energy transmission," *IEEE Transactions on Industrial Electronics*, vol. 66, no. 7, pp. 5289-5299, Jul. 2019.

[8] Y. Chang and X. Cai, "Hybrid topology of a diode-rectifier-based HVDC system for offshore wind farms," *IEEE Journal of Emerging and Selected Topics in Power Electronics*, vol. 7, no. 3, pp. 2116-2128, Sept. 2019.

[9] Y. Jin, Z. Zhang, and Z. Xu, "Proportion of grid-forming wind turbines in hybrid GFM-GFL offshore wind farms integrated with diode rectifier unit based HVDC system," *Journal of Modern Power Systems and Clean Energy*. DOI: 10.35833/MPCE.2024.000432

[10] R. Blasco-Gimenez, S. Añó -Villalba, J. Rodríguez-D'Derlée *et al*., "Distributed voltage and frequency control of offshore wind farms connected with a diode-based HVDC link," *IEEE Transactions on Power Electronics*, vol. 25, no. 12, pp. 3095-3105, Dec. 2010.

[11] Z. Zhang, Y. Tang, and Z. Xu, "Medium frequency diode rectifier unit based HVDC transmission for offshore wind farm integration," *IET Renewable Power Generation*, vol. 15, no. 4, pp. 717-730, Mar. 2021.

[12] Y. Tang, Z. Zhang, and Z. Xu, "DRU based low frequency AC transmission scheme for offshore wind farm integration," *IEEE Transactions on Sustainable Energy*, vol. 12, no. 3, pp. 1512-1524, Jul. 2021.

[13] L. Yu, R. Li, L. Xu *et al*., "Analysis and control of offshore wind farms connected with diode rectifier-based HVDC system," *IEEE Transactions on Power Delivery*, vol. 35, no. 4, pp. 2049-2059, Aug. 2020.

[14] L. Yu, L. Xu, J. Zhu *et al*., "Impedance modelling and stability analysis of diode-rectifier based HVDC connected offshore wind farms," *IEEE Transactions on Power Delivery*, vol. 37, no. 1, pp. 591-602, Feb. 2022.

[15] H. Xiao, X. Huang, Y. Huang *et al*., "Self-synchronizing control and frequency response of offshore wind farms connected to diode rectifier based HVDC system," *IEEE Transactions on Sustainable Energy*, vol. 13, no. 3, pp. 1681-1692, Jul. 2022.

[16] Z. Zhang, Y. Jin, and Z. Xu, "Grid-forming control of wind turbines for diode rectifier unit based offshore wind farm integration," *IEEE Transactions on Power Delivery*, vol. 38, no. 2, pp. 1341-1352, Apr. 2023.

[17] IEA. (2021, Aug.). Renewables 2021 analysis and forecast to 2026. [Online]. Available: https://www.iea.org/reports/renewables-2021

[18] P. Meng, W. Xiang, and J. Wen, "Communication-less reactive power control of grid-forming wind turbines connected to cascaded LCC-DR HVDC system," *IEEE Transactions on Power Systems*, vol. 39, no. 5, pp. 6740-6752, Sept. 2024.

[19] R. Blasco-Gimenez, N. Aparicio, S. Ano-Villalba *et al*., "LCC-HVDC connection of offshore wind farms with reduced filter banks," *IEEE Transactions on Industrial Electronics*, vol. 60, no. 6, pp. 2372-2380, Jun. 2013.

[20] A. Bidadfar, O. Saborio-Romano, N. A. Cutululis *et al*., "Control of offshore wind turbines connected to diode-rectifier-based HVDC systems," *IEEE Transactions on Sustainable Energy*, vol. 12, no. 1, pp. 514-523, Jan. 2021.

[21] G. Zhang, W. Xiang, X. Chen *et al*., "Capacity design of cascaded diode rectifier-MMC based HVDC for offshore wind farm integration," *IEEE Transactions on Power Delivery*, vol. 39, no. 5, pp. 2908-2919,

Oct. 2024.
[22] M. A. Cardiel-Alvarez, S. Arnaltes, J. L. Rodriguez-Amenedo *et al*., "Decentralized control of offshore wind farms connected to diode-based HVDC links," *IEEE Transactions on Energy Conversion*, vol. 33, no. 3, pp. 1233-1241, Sept. 2018.
[23] Y. Wang, J. Meng, X. Zhang *et al*., "Control of PMSG-based wind turbines for system inertial response and power oscillation damping," *IEEE Transactions on Sustainable Energy*, vol. 6, no. 2, pp. 565-574, Apr. 2015.
[24] E. Muljadi, S. Pasupulati, A. Ellis *et al*., "Method of equivalencing for a large wind power plant with multiple turbine representation," in *Proceedings of 2008 IEEE PES General Meeting*, Pittsburgh, USA, Jul. 2008, pp. 1-9.
[25] G. Zhang, W. Xiang, and J. Wen, "Impedance modeling and stability analysis of DR-MMC based hybrid HVDC for offshore wind farm integration," *IEEE Transactions on Power Delivery*, vol. 38, no. 6, pp. 4397-4409, Dec. 2023.
[26] K. Ji, G. Tang, H. Pang *et al*., "Impedance modeling and analysis of MMC-HVDC for offshore wind farm integration," *IEEE Transactions on Power Delivery*, vol. 35, no. 3, pp. 1488-1501, Jun. 2020.
[27] Y. Li and Z. Du, "Stabilizing condition of grid-connected VSC as affected by phase locked loop," *IEEE Transactions on Power Delivery*, vol. 37, no. 2, pp. 1336-1339, Apr. 2022.

Ganghua Zhang received the B. S. degree in electrical engineering from South China University of Technology, Guangzhou, China, in 2020. He is currently working toward the Ph.D. degree in electrical engineering at Huazhong University of Science and Technology, Wuhan, China. His main research interests include DC grid, modeling and stability analysis of grid-integrated renewable energy system.

Wang Xiang received the B.Eng. and Ph.D. degrees in electrical engineering from Huazhong University of Science and Technology, Wuhan, China, in 2012 and 2017, respectively. He was a visiting Ph.D. student at the University of Aberdeen, Aberdeen, UK and the University of Strathclyde, Glasgow, UK, in 2014 and 2016, respectively. He was with the University of Strathclyde from 2018 to 2021. Currently, he is a Professor at School of Electrical and Electronics Engineering, Huazhong University of Science and Technology. His main research interests include modular multilevel converter based high-voltage direct current (MMC-HVDC), high-power DC/DC converter, DC grid, and offshore wind power integration.

Xia Chen received the B.S. degree in power system and its automaton from Wuhan University of Technology, Wuhan, China, in 2006, and the M.S. and Ph. D. degrees in electrical engineering from Huazhong University of Science and Technology (HUST), Wuhan, China, in 2008 and 2012, respectively. From 2012 to 2015, she was a Postdoctoral Research Fellow with The University of Hong Kong, Hong Kong, China. In 2015, she joined HUST, where she is currently a Professor with the School of Electrical and Electronic Engineering. Her main research interests include distributed control technology in microgrid, renewable energy integration technology, and smart grid device.

Rui Tu received the B.S. degree in electrical engineering from North China Electric Power University, Beijing, China, in 2023. She is currently working toward the Ph.D. degree in electrical engineering at Huazhong University of Science and Technology, Wuhan, China. Her main research interests include MMC-HVDC and offshore wind power integration.

Xuebo Qiao received the B.S., M.S., and Ph.D. degrees in electrical engineering from Hunan University, Changsha, China, in 2015, 2018, and 2022, respectively. He is currently working as a Research Fellow in electrical engineering at Huazhong University of Science and Technology, Wuhan, China. His research interests include high-voltage direct current (HVDC) technology and grid connection and transmission technology of offshore wind power.

Jinyu Wen received the B.Eng. and Ph.D. degrees in electrical engineering from Huazhong University of Science and Technology (HUST), Wuhan, China, in 1992 and 1998, respectively. He was a visiting student from 1996 to 1997 and Research Fellow from 2002 to 2003 at the University of Liverpool, Liverpool, UK, and a Senior Visiting Researcher at the University of Texas at Arlington, Arlington, USA, in 2010. From 1998 to 2002, he was a Director Engineer in XJ Electric Co., Ltd., Xuchang, China. In 2003, he joined the HUST and now is a Professor at HUST. His current research interests include renewable energy integration, energy storage application, DC grid, and power system operation and control.